


ARTICLE

Open Access

# Smart polymer-based calcium-ion self-regulated nanochannels by mimicking the biological $\text{Ca}^{2+}$ -induced $\text{Ca}^{2+}$ release process

Yunlong Li<sup>1,2</sup>, Yuting Xiong<sup>2</sup>, Dongdong Wang<sup>2</sup>, Xiuling Li<sup>2</sup>, Zhixiang Chen<sup>1,2</sup>, Cunli Wang<sup>2</sup>, Haijuan Qin<sup>3</sup>, Jinxuan Liu<sup>4</sup>, Baisong Chang<sup>1</sup> and Guangyan Qing<sup>1</sup> 

## Abstract

In nature, ion channels play key roles in controlling ion transport between cells and their surroundings. Calcium ion ( $\text{Ca}^{2+}$ )-induced  $\text{Ca}^{2+}$  release (CICR), a critical control mechanism for  $\text{Ca}^{2+}$  channels, occurs due to a  $\text{Ca}^{2+}$  concentration gradient working in synergy with ryanodine receptors, which are famously known as “calcium sparks”. Inspired by this self-regulated biological process, a smart  $\text{Ca}^{2+}$  concentration-modulated nanochannel system was developed by integrating a poly(*N*-isopropylacrylamide-*co*-acrylamide-[4-(trifluoromethyl) phenyl]-2-thiourea<sub>0.2</sub>-*co*-acrylamide-DDDEEK<sub>0.2</sub>) (denoted as PNI-*co*-CF<sub>3</sub>-PT<sub>0.2</sub>-*co*-DDDEEK<sub>0.2</sub>) three-component copolymer onto the nanochannels of a porous anodic alumina (PAA) membrane. In this smart polymer design, the DDDEEK hepta-peptide unit has an extraordinary binding affinity with  $\text{Ca}^{2+}$  through coordination bonds, while CF<sub>3</sub>-PT functions as a hydrogen bond mediation unit, facilitating the remarkable conformational transition of the PNI main chain in response to  $\text{Ca}^{2+}$ -specific adsorption. Due to these features, the dynamic gating behaviors of the modified nanochannels could be precisely manipulated by the  $\text{Ca}^{2+}$  concentration. In addition, the sensitive  $\text{Ca}^{2+}$  response, as low as 10 pM with a high specificity toward  $\text{Ca}^{2+}$  capable of discriminating  $\text{Ca}^{2+}$  from other potential interference metal ions (e.g., K<sup>+</sup>, Cu<sup>2+</sup>, Mg<sup>2+</sup>, Zn<sup>2+</sup>, Fe<sup>3+</sup>, and Al<sup>3+</sup>), remarkable morphological change in the nanochannel and satisfactory reversibility indicate the great potential of  $\text{Ca}^{2+}$ -responsive polymers for the fabrication of biodevices and artificial nanochannels.

## Introduction

Natural ion channels, with high fidelity to specific ions, act as a pivotal part in supporting the metabolism of living cells (Scheme 1), and their dysfunction can lead to various diseases<sup>1,2</sup>; 40% of clinical drugs are designed to target ion channel proteins. Among ion channels,  $\text{Ca}^{2+}$  channels are prerequisites for an extensive range of life processes<sup>3,4</sup>,

such as functions of nervous systems, cell proliferation, genetic transcription, and muscular contraction<sup>5,6</sup>. In particular, ryanodine receptors (RyRs) on sarcoplasmic reticulum (SR) membranes, which are in charge of the release of intracellular  $\text{Ca}^{2+}$  stores, are sensitive to the concentration of  $\text{Ca}^{2+}$  (Scheme 1, the lower part). Once the concentration reaches a threshold ( $10^{-6}$ – $10^{-5}$  mol L<sup>-1</sup> (M)), conformational switching of RyRs will occur, which increases the helicity of the protein and shortens the distance and dihedral angle between two S6-peptide chains (Scheme 2a)<sup>7–9</sup>, resulting in the opening of nanopores of RyRs and the release of a large number of  $\text{Ca}^{2+}$  ions from the SR. These released  $\text{Ca}^{2+}$  will bind with calmodulin protein, subsequently leading to the closure of

Correspondence: Guangyan Qing ([qinggy@dicp.ac.cn](mailto:qinggy@dicp.ac.cn))

<sup>1</sup>State Key Laboratory of Advanced Technology for Materials Synthesis and Processing, Wuhan University of Technology, 122 Luoshi Road, 430070 Wuhan, PR China

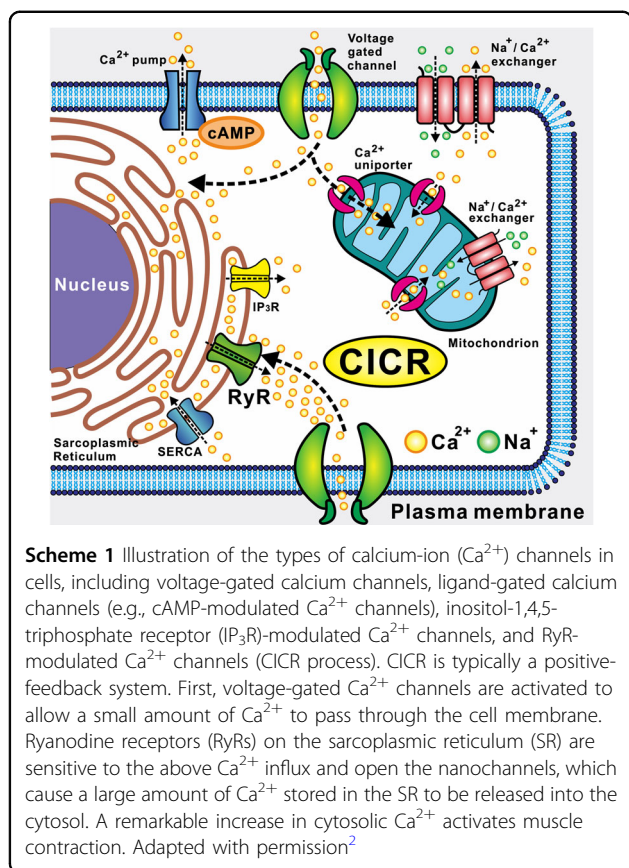
<sup>2</sup>Key Laboratory of Separation Science for Analytical Chemistry, Dalian Institute of Chemical Physics, Chinese Academy of Sciences, 457 Zhongshan Road, 116023 Dalian, PR China

Full list of author information is available at the end of the article.

© The Author(s) 2019

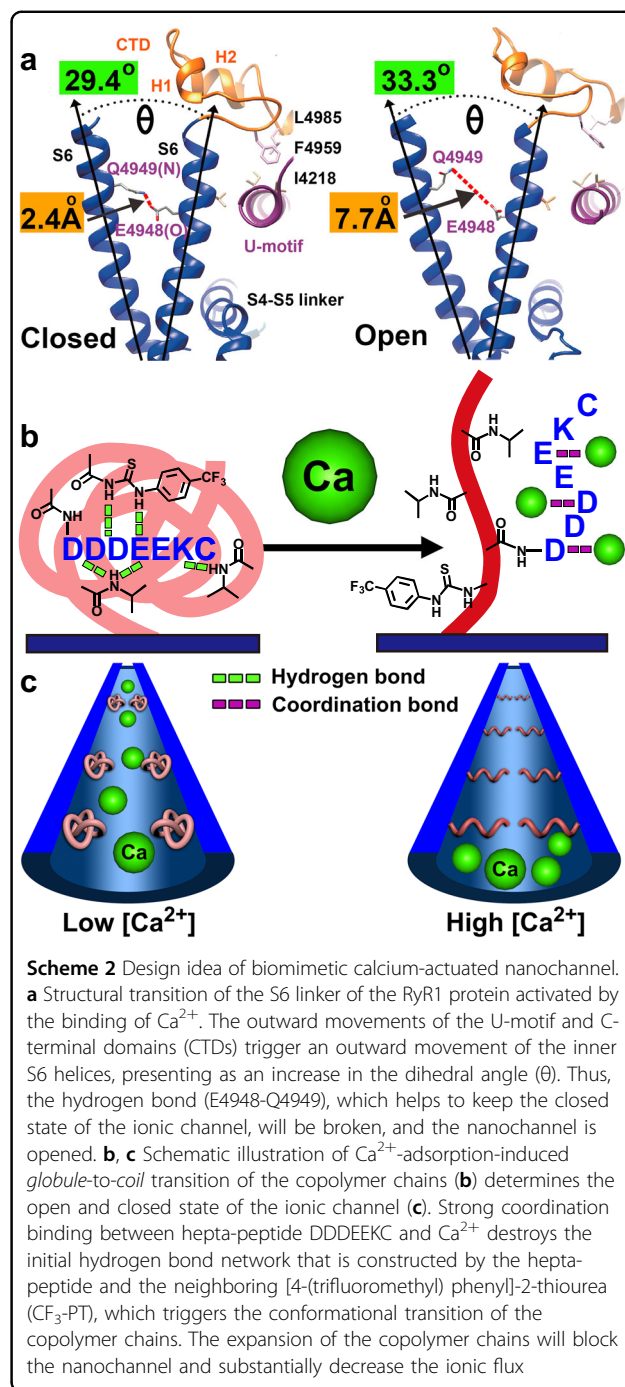


**Open Access** This article is licensed under a Creative Commons Attribution 4.0 International License, which permits use, sharing, adaptation, distribution and reproduction in any medium or format, as long as you give appropriate credit to the original author(s) and the source, provide a link to the Creative Commons license, and indicate if changes were made. The images or other third party material in this article are included in the article's Creative Commons license, unless indicated otherwise in a credit line to the material. If material is not included in the article's Creative Commons license and your intended use is not permitted by statutory regulation or exceeds the permitted use, you will need to obtain permission directly from the copyright holder. To view a copy of this license, visit <http://creativecommons.org/licenses/by/4.0/>.



the  $\text{Ca}^{2+}$  channel. Thus, a  $\text{Ca}^{2+}$ -induced  $\text{Ca}^{2+}$  release (CICR) process proceeds, which is crucial to the maintenance of the intracellular  $\text{Ca}^{2+}$  concentration and controls muscle contraction, particularly the cardiac muscle. The malfunction of the CICR process can lead to a great number of serious diseases<sup>10,11</sup>. This unique biological event has inspired chemists to develop various  $\text{Ca}^{2+}$ -sensitive ion channels and nanodevices<sup>12–14</sup>.

In the past decade, several elegant approaches have been applied to construct  $\text{Ca}^{2+}$ -modulated nanochannels<sup>15–17</sup>. As typical examples, Siwy et al.<sup>18</sup> reported a  $\text{Ca}^{2+}$ -induced voltage gating, ionic current oscillations<sup>19</sup>, and charge inversion<sup>20</sup>, on the basis of track-etched asymmetric nanopores on polyethylene terephthalate (PET) films. Meng et al.<sup>21</sup> utilized calcein-modified PET nanochannels to achieve a  $\text{Ca}^{2+}$ -responsive nanogating. These modulation strategies mainly rely on surface charge changes of the nanochannels to achieve “on–off” switching, which are different from the ion channels in vivo whose gating behaviors are mainly achieved by the conformational transition of channel proteins, as illustrated in Scheme 2a. Within this context, much attention has been devoted to smart polymer-based<sup>22</sup> nanochannels, which bear the obvious advantages of high controllability, satisfactory reversibility, and remarkable conformational transition in



response to external stimuli<sup>23,24</sup>. By producing diverse external stimuli, such as temperature, pH, light, or redox potential<sup>25–27</sup>, reversible tuning of ion transport across smart polymer-modified nanochannels can be achieved, which has resulted in wide applications for both material sciences and life sciences<sup>28–32</sup>.

Nevertheless, to the best of our knowledge, smart polymer-based nanochannels that can be manipulated by  $\text{Ca}^{2+}$  concentration have rarely been reported. Building

biomimetic  $\text{Ca}^{2+}$ -sensitive ion channels is important for simulating the self-regulating and gating behaviors of RyR channels, the largest known calcium ion channel in humans. These channels will contribute to a more comprehensive understanding of  $\text{Ca}^{2+}$  signal pathways and promote numerous interesting applications in tissue engineering, controllable drug release, bioseparation, biosensors, microfluidics, and microreactors<sup>33</sup>.

Herein, inspired by the CICR process, a biomimetic  $\text{Ca}^{2+}$  self-regulated nanochannel system is constructed based on a  $\text{Ca}^{2+}$ -responsive polymer design. A three-component copolymer PNI-*co*- $\text{CF}_3$ -PT<sub>0.2</sub>-*co*-DDDEEK<sub>C</sub><sub>0.2</sub> was designed according to a “recognition–mediation–main chain” concept<sup>34,35</sup>, in which the hepta-peptide DDDEEK works as a  $\text{Ca}^{2+}$ -recognition unit,  $\text{CF}_3$ -PT functions as a hydrogen-bond mediation unit and PNI provides a flexible polymer main chain. As the core recognition unit for  $\text{Ca}^{2+}$ , DDDEEK with an  $\alpha$ -helix conformation was first found as an *N*-terminal region of statherin<sup>36</sup> with a strong adsorption capacity toward hydroxyapatite, which inspired us to utilize this natural peptide to design the  $\text{Ca}^{2+}$ -binding material<sup>37,38</sup>. Subsequently,  $\text{CF}_3$ -PT was introduced as a mediation unit owing to its strong hydrogen bond donating capacity. The thiourea group in  $\text{CF}_3$ -PT can combine with the carboxyl groups in the above hepta-peptide utilizing multiple hydrogen bonding interactions to build a compact hydrogen bond network within the copolymer, as shown in Scheme 2b in the left panel. When the copolymer film is exposed to  $\text{Ca}^{2+}$ , multiple and strong chelation bindings between  $\text{Ca}^{2+}$  and the carboxyl groups in the hepta-peptide gradually destroy the initial hydrogen bond network. When the  $\text{Ca}^{2+}$  concentration reaches a threshold, the copolymer chains undergo a dramatic *globule*-to-*coil* transition, leading to an obvious expansion of the copolymer film (Scheme 2b, right panel). This smart polymer design not only improves the grafting density of the core hepta-peptide to provide more binding sites for  $\text{Ca}^{2+}$  but also supplies an ideal platform to amplify the  $\text{Ca}^{2+}$  recognition signal by taking advantage of the conformational transition of the copolymer chain. The combination of these two merits can substantially improve the sensitivity of the material.

Then, porous anodic alumina (PAA) was chosen as a substrate to build the nanochannel system. Compared with other porous materials, PAA exhibits remarkable advantages, such as adjustable film thickness, high porosity, and tunable parameters, and has been widely used in controlling ion transportation, as well as constructing various functional devices<sup>39–41</sup>. By using surface-initiated atom transfer radical polymerization (SI-ATRP)<sup>42,43</sup>, the designed copolymer was then immobilized onto the straight-through nanochannel of a PAA membrane with an average diameter ranging from 70 to 100 nm. The affinity test, quartz crystal microbalance with dissipation (QCM-D) binding analysis, electrochemical impedance

spectroscopy (EIS) analysis, morphological observations, and transmembrane ionic current measurements clearly demonstrated that the well-developed nanochannel displayed controllable and reversible gating abilities toward  $\text{Ca}^{2+}$  adsorption or desorption, as illustrated in Scheme 2c. It is worth noting that such a gating effect was highly specific to  $\text{Ca}^{2+}$ , and other metal ions, such as  $\text{K}^+$ ,  $\text{Mg}^{2+}$ ,  $\text{Al}^{3+}$ ,  $\text{Zn}^{2+}$ ,  $\text{Fe}^{3+}$ , and  $\text{Cu}^{2+}$ , did not induce any evidential changes. This work provides a smart polymer-based design concept to mimic the crucial CICR process; precise  $\text{Ca}^{2+}$ -modulated gating performance might facilitate the development of various bioseparation membranes, nanochannels, and microfluidic devices<sup>44</sup>.

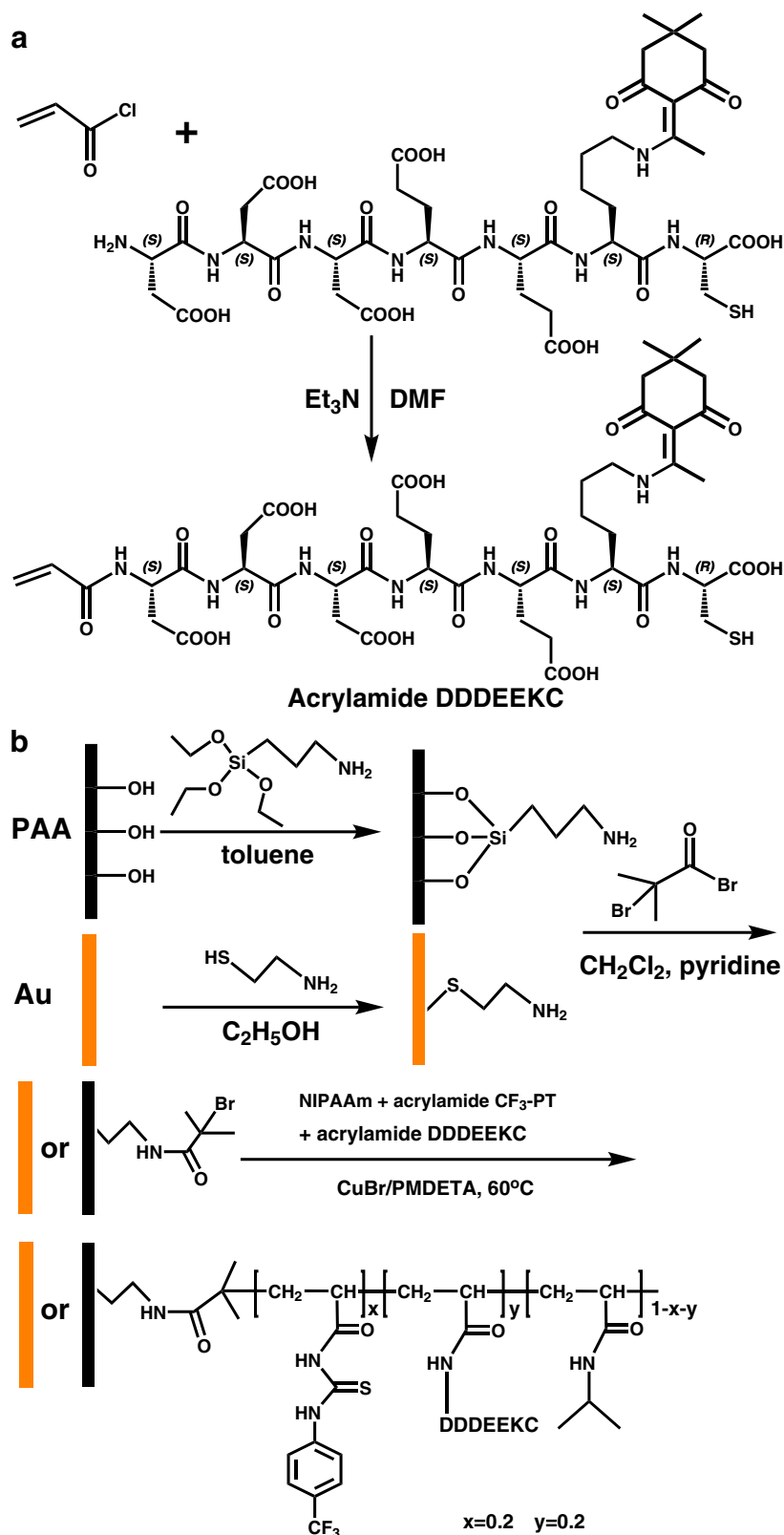
## Materials and methods

### Materials

*N*-Isopropylacrylamide (NIPAAm, 98%) was purchased from Sigma-Aldrich (China) and was recrystallized in *n*-hexane three times before being used in the copolymerization. The peptide sequence DDDEEK(Dde)C was purchased from ChinaPeptides Co., LTD with high purity (>99%). 2-Bromoisobutyryl bromide, 2-mercaptoethylamine, and *N,N,N',N'',N'''*-penta-methyldiethylenetriamine (PMDETA) (Sigma-Aldrich) were used as received.

### Synthesis of acrylamide hepta-peptide

The synthesis of acrylamide hepta-peptide was illustrated in Scheme 3a. DDDEEK(Dde)C (0.204 g, 0.2 mmol) and 0.2 mL triethylamine were dissolved in 15 mL anhydrous *N,N'*-dimethylformamide (DMF), and the mixture was stirred for 15 min in an ice bath. Then, 5 mL of DMF containing acryloyl chloride (0.035 mL, 0.4 mmol) was added to the mixture dropwise and stirred for 0.5 h in an ice bath. The reaction mixture was then stirred at room temperature for 24 h. Most DMF was evaporated under reduced pressure. The crude product was purified on a Shimadzu UFLC 20A purity system with a C18 reverse-phase semipreparative chromatographic column. The pure product was obtained as a white powder (0.142 g, yield: 66%). <sup>1</sup>H NMR (*d*<sub>6</sub>-DMSO)  $\delta$  (ppm): 13.23 (s, 2H, COOH), 12.00–12.50 (br, 4H, COOH), 9.35–9.53 (m, 6H, CONH), 6.23 (d, *J* = 17.2 Hz, 1H, CH = C), 6.05, 6.09 (dd, *J*<sub>1</sub> = *J*<sub>2</sub> = 10 Hz, 1H, CH = C), 5.86 (d, *J* = 10.4 Hz, 1H, CH = C), 4.46–4.58 (m, 2H, \*CH), 4.30–4.39 (m, 2H, \*CH), 4.19–4.28 (m, 3H, \*CH), 3.06–3.10 (m, 16H, CH<sub>2</sub>C, 3H, CCH<sub>3</sub>), 2.47 (s, 2H, Dde-COCH<sub>2</sub>), 2.27 (s, 2H, Dde-COCH<sub>2</sub>), 1.85–1.93 (m, 2H, CH<sub>2</sub>C), 1.67–1.77 (m, 2H, CH<sub>2</sub>C), 1.53–1.60 (m, 2H, CH<sub>2</sub>C), 1.32–1.39 (m, 2H, CH<sub>2</sub>C), 0.94 (s, 6H, Dde-CCH<sub>3</sub>). Elemental analysis, calcd. (%) for C<sub>44</sub>H<sub>62</sub>N<sub>8</sub>O<sub>21</sub>S: C, 49.34; H, 5.83; N, 10.46; found C, 49.21; H, 5.75; N, 10.63; MALDI-MS: *m/z* calcd. for C<sub>44</sub>H<sub>62</sub>N<sub>8</sub>O<sub>21</sub>S: 1070.38; found: 1071.37 [M + H]<sup>+</sup>.



**Scheme 3 a** Preparation of acrylamide DDDEEK(Dde)C. **b** Modification of porous anodic alumina (PAA) membrane, gold surface of QCM-D resonator, or electrode with poly[*N*-isopropylacrylamide-*co*-acrylamide 1-[4-(trifluoromethyl)phenyl]-2-thiourea<sub>0.2</sub>-*co*-acrylamide-DDDEEK<sub>0.2</sub>] (denoted as PNI-*co*-CF<sub>3</sub>-PT<sub>0.2</sub>-*co*-DDDEEK<sub>0.2</sub>) via surface-initiated atom transfer radical polymerization



### Synthesis of PNI-co-CF<sub>3</sub>-PT<sub>0.2</sub>-co-DDDEEK<sub>0.2</sub>-modified PAA membrane

For the modification of the PAA membrane (Scheme 3b), the PAA membrane was first immersed in distilled water and ethanol for 10 min, followed by a quick dip in a hydrochloric acid aqueous solution (5%, v/v) for 35 s and subsequently in hydrogen peroxide heated at 100 °C for 1 h to generate surface hydroxyl groups. After that, the membrane was washed with an excess of distilled water and ethanol and dried under a nitrogen flow. Then, it was heated at 65 °C in 40 mL toluene containing 1.0 mL APTES for 3 h to obtain chemically bonded-NH<sub>2</sub> groups on the membranes. The reaction was performed in a nitrogen atmosphere. Ethanol was used to wash out the remaining APTES. After drying under a flow of nitrogen gas, the PAA membrane was immersed in 50 mL dry dichloromethane containing 0.4 mL pyridine. Then, 2-bromoisobutryl bromide (0.4 mL) was added dropwise into the solvent at 0 °C for 1 h, and then at 25 °C for 12 h. After rinsing with CH<sub>2</sub>Cl<sub>2</sub>, a bromine-modified PAA membrane was received.

The modifications of PNI-co-CF<sub>3</sub>-PT<sub>0.2</sub>-co-DDDEEK<sub>0.2</sub> were synthesized by the method of ATRP according to the literature<sup>43</sup>. The bromine-modified PAA membrane was immersed in a degassed solution of NIPAM (0.1371 g, 1.2 mmol), acrylamide CF<sub>3</sub>-PT (0.1096 g, 0.4 mmol), acrylamide-DDDEEK (0.4284 g, 0.4 mmol) in 10 mL DMF containing CuBr (0.0143 g, 0.1 mmol), and *N,N,N',N',N'*-PMDETA (0.1 mL, 0.47 mmol). The reaction was carried out at 60 °C for 15 h with nitrogen protection. Subsequently, the copolymer-modified PAA membrane was sequentially cleaned with DMF, water, and ethanol and subsequently dried under a nitrogen flow. The PNIPAAm-modified and CF<sub>3</sub>-PT-co-DDDEEK-modified PAA membranes were prepared through a method similar to that described above.

### Electrical measurements

#### Electrochemical impedance spectroscopy measurement

EIS experiments were performed in 0.1 mmol L<sup>-1</sup> KCl solution containing [Fe(CN)<sub>6</sub>]<sup>3-/4-</sup> (5 mmol L<sup>-1</sup>), and the experimental conditions were as follows: open circuit potential, 0.3 V; alternative voltage, 5 mV; frequency range, 0.1–10<sup>5</sup> Hz. The PNI-co-CF<sub>3</sub>-PT<sub>0.2</sub>-co-DDDEEK<sub>0.2</sub>-modified Au electrode was prepared using the same method described above. The working electrode, which was a Au electrode modified with PNI-co-CF<sub>3</sub>-PT<sub>0.2</sub>-co-DDDEEK<sub>0.2</sub>, a Ag/AgCl reference electrode and a graphite auxiliary electrode made up the three-electrode system. Temperature: 20 °C.

#### Ionic current measurement

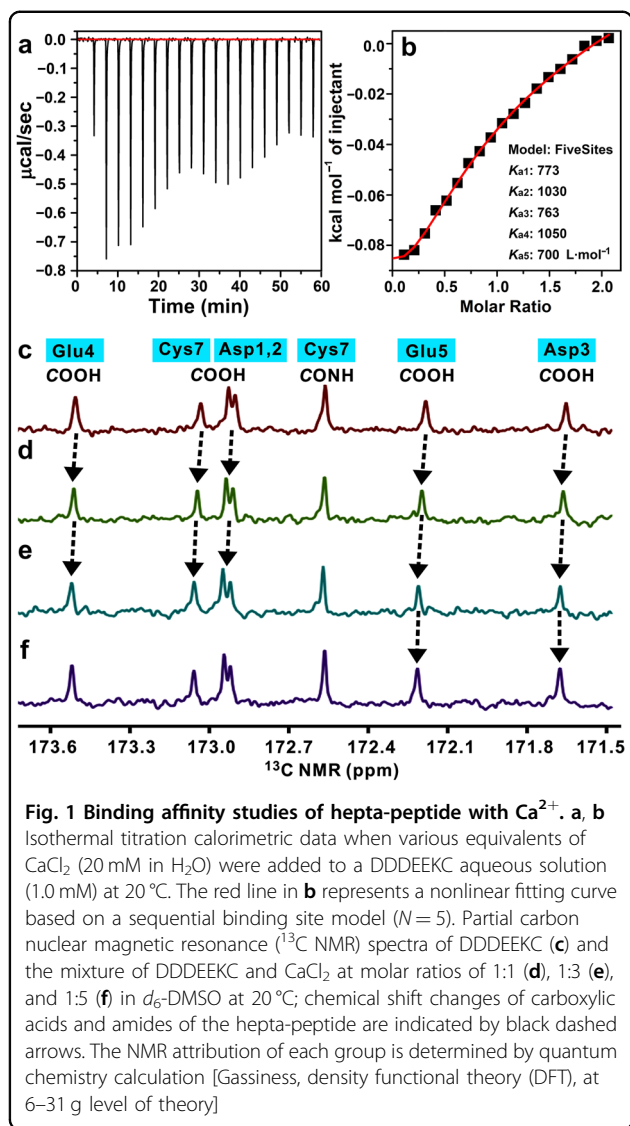
A piece of PAA membrane (bare or modified) was mounted between a two-compartment electrochemical

cell according to the literature<sup>45</sup>. Ag/AgCl electrodes were used to apply a transmembrane potential across the membrane. The transmembrane ionic current was measured with a Keithley 6487 picoammeter/voltage source (Keithley Instruments) through Ag/AgCl electrodes. The effective area for the ionic conduction measurements was ~20 mm<sup>2</sup>. The electrolyte was 0.01 M sodium chloride (NaCl) solution.

### Results

First, the binding affinity of the hepta-peptide with CaCl<sub>2</sub> was evaluated by isothermal titration calorimetry (ITC), which has been widely used as a label-free and quantitative technique to detect the thermodynamic parameters of interactions between a small molecule and a biomacromolecule in solution<sup>46</sup>. A classical isothermal calorimetric titration profile of 20 mM Ca<sup>2+</sup> with 1 mM hepta-peptide in pure water at 25 °C is shown in Fig. 1a. Strong heat release was observed, corresponding to an ~5:1 binding stoichiometry between Ca<sup>2+</sup> and hepta-peptide with stepwise binding constants of *K*<sub>a1</sub>, 773; *K*<sub>a2</sub>, 1030; *K*<sub>a3</sub>, 763; *K*<sub>a4</sub>, 1050; and *K*<sub>a5</sub>, 700 L mol<sup>-1</sup> (Fig. 1b), as well as a accumulative *K*<sub>a</sub> (*K*<sub>a1</sub> × *K*<sub>a2</sub> × *K*<sub>a3</sub> × *K*<sub>a4</sub> × *K*<sub>a5</sub>) of 4.46 × 10<sup>14</sup> L mol<sup>-1</sup>, which suggested strong and specific complexation. Carbon nuclear magnetic resonance (<sup>13</sup>C NMR) titration experiments validated this complexation. As shown in Fig. 1c–f, upon the addition of different amounts of CaCl<sub>2</sub> to the hepta-peptide in deuterated water, six sets of carbon atom signals for carboxyl groups in the hepta-peptide display clear downfield shifts. By comparison, no obvious chemical shift change was observed for the carbon atom signals of the amide groups. This difference indicated that multiple coordination bonds between Ca<sup>2+</sup> and the carboxyl groups in the hepta-peptide were the main driving forces for the strong complexation.

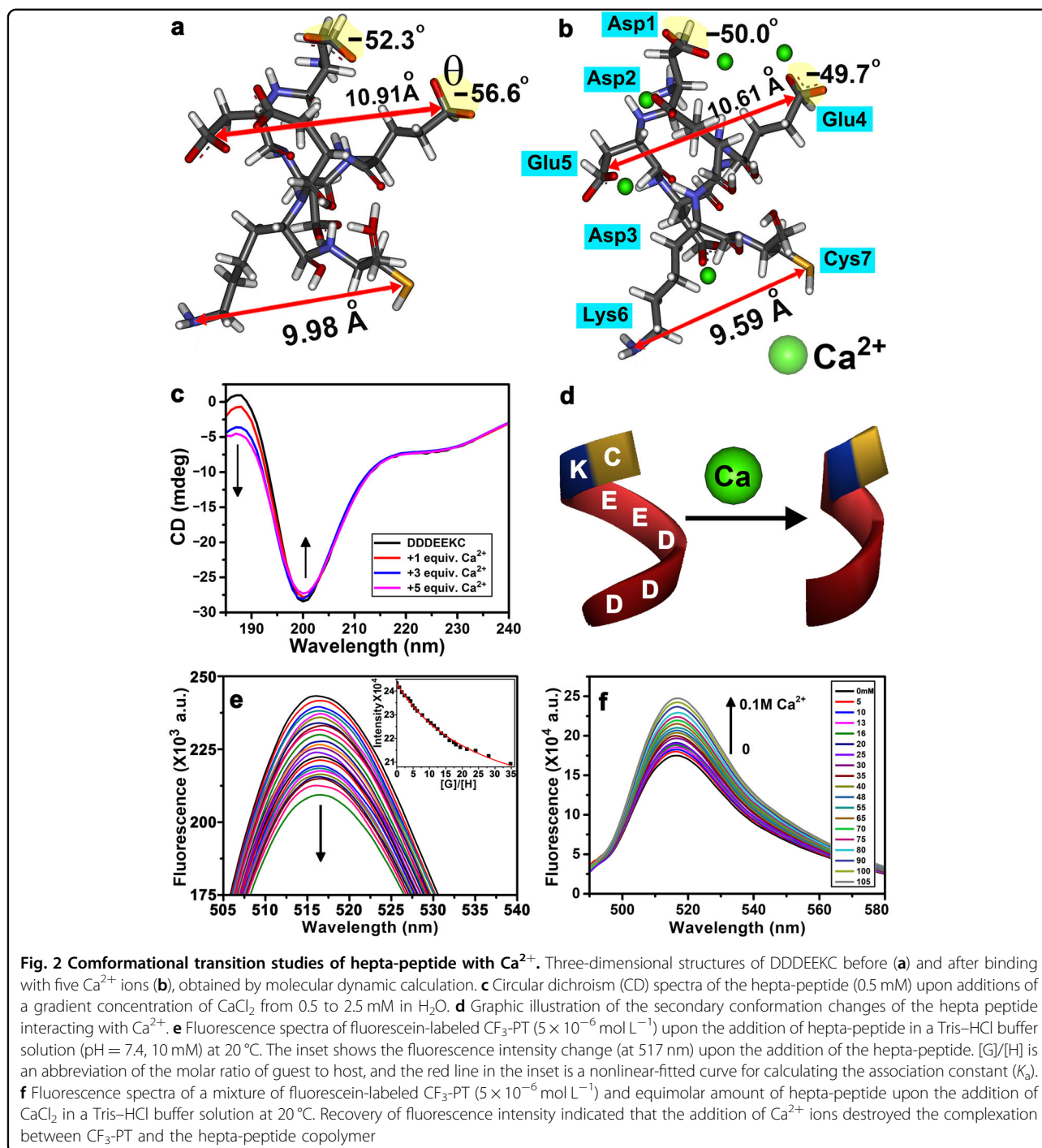
A possible binding model was provided by molecular dynamic calculations by using the density function theory. Figure 2a, b shows three-dimensional structures of the hepta-peptide before and after interacting with five Ca<sup>2+</sup>, and some remarkable changes in peptide conformation and dihedral angle (θ) of the carboxyl group could be observed. Specifically, the distance between the amine in the side chain of the sixth Lys and the thiol in the seven Cys decreases from 9.98 to 9.59 Å, while the distance between the carboxyl groups in the fourth Glu and the fifth Glu decreases from 10.97 to 10.61 Å. The dihedral angle of the carboxyl group in the fifth Glu displays a noteworthy increase from -31° to -39° after binding with Ca<sup>2+</sup>. Circular dichroism (CD) was applied to further discuss the conformation change of the hepta-peptide. The CD spectrum of the hepta-peptide was similar to that observed for α-helical polypeptides according to the literature<sup>47,48</sup>. Although the banding intensity may vary with



solvents due to the different polarity and hydrogen bonding strength, a strong negative adsorption peak centered at 200 nm and a weak shoulder peak at ~225 nm could be observed, which represent the exciton split of the  $\pi$ - $\pi^*$  and  $n$ - $\pi$  at the long wavelength component, respectively (Fig. 2c). Upon the addition of  $\text{CaCl}_2$  to the hepta-peptide solution, the CD intensity of the peak at 200 nm decreases slightly, while the signal at 188 nm increases, which indicated a decrease in the proportion of the  $\alpha$ -helix structure and the appearance of a random coil structure due to competitive binding interactions between hepta-peptide and the  $\text{CaCl}_2$  solute. The remarkable conformational change (Fig. 2d) and high affinity measured by the ITC and  $^{13}\text{C}$  NMR titration experiments revealed that this hepta-peptide can serve as an ideal binding unit for  $\text{Ca}^{2+}$ .

For the purpose of improving the binding affinity with  $\text{Ca}^{2+}$  and amplifying the recognition signal, the acrylamide hepta-peptide was prepared to copolymerize with acrylamide  $\text{CF}_3$ -PT and NIPAAm through SI-ATRP, generating a smart PNI-*co*- $\text{CF}_3$ -PT<sub>0.2</sub>-*co*-DDDEEKC<sub>0.2</sub> copolymer film (average thickness of 20 nm) on a QCM resonator gold electrode surface. The grafting ratios of 0.2 for hepta-peptide and  $\text{CF}_3$ -PT units were determined according to the elemental analysis and integration ratios of the characteristic peaks in the  $^1\text{H}$  NMR spectrum of the copolymer (Supplementary Fig. 2a in SI). To test the three-component copolymer design (Scheme 2b), a fluorescence titration experiment was performed to evaluate the binding affinity ( $K_a$ )<sup>49</sup> between a fluorescein-labeled  $\text{CF}_3$ -PT (Supplementary Fig. 1 in SI) and the hepta-peptide. As shown in Fig. 2e, when 35 equivalents of hepta-peptide were added into the fluorescein-labeled  $\text{CF}_3$ -PT ( $5 \times 10^{-6}$  mol  $\text{L}^{-1}$ ) in Tris-HCl buffer solution (pH 7.4, 10 mM), and the fluorescence intensity of the solution decreased by 14%, corresponding to a  $K_a$  of  $7969 \pm 480$   $\text{L mol}^{-1}$  calculated from a nonlinear fitting. It is worth noting that such a fluorescence intensity decrease was not caused by the acidity of the carboxyl groups in the hepta-peptide because the solution pH was maintained at a constant value by a buffer solution. Then, an equimolar mixture of the hepta-peptide and the fluorescein-labeled  $\text{CF}_3$ -PT in Tris-HCl buffer solution was prepared, and the fluorescence spectra were recorded (Fig. 2f). Interestingly, when different amounts of  $\text{CaCl}_2$  capable of binding with the hepta-peptide were added to the mixture, the fluorescence intensity of  $\text{CF}_3$ -PT increased gradually and returned to its initial value prior to the hepta-peptide addition. The recovery of fluorescence intensity could be reasonably attributed to the competitive binding of the hepta-peptide with  $\text{Ca}^{2+}$ , which was substantially stronger than that of the hepta-peptide with  $\text{CF}_3$ -PT<sup>50,51</sup>. Attenuated total reflection fourier transform infrared spectroscopy (ATR-IR) further validated the interaction between the hepta-peptide and  $\text{CF}_3$ -PT (Supplementary Fig. 3 in SI).

The above control experiment demonstrated the feasibility of our smart polymer design. Then, the adsorption dynamics of various metal ions on the PNI-*co*- $\text{CF}_3$ -PT<sub>0.2</sub>-*co*-DDDEEKC<sub>0.2</sub> copolymer surface were monitored using a QCM-D to measure the frequency ( $\Delta f$ ) and energy dissipation ( $\Delta D$ )<sup>52</sup>. As shown in Fig. 3a by the red line,  $\text{CaCl}_2$  (10  $\mu\text{M}$  in pure water) displays slow and strong adsorption on the copolymer surface and reaches a maximum after 45 min ( $\Delta f = 32.5$  Hz); according to the Sauerbrey equation<sup>53</sup>, the adsorption quantity is 191.5  $\text{ng cm}^{-2}$ . Under the same conditions, the  $\text{FeCl}_3$ -induced frequency change was only -3.8 Hz, and NaCl, KCl, or  $\text{AlCl}_3$ -induced frequency changes were negligible. Interestingly, the adsorption of  $\text{MgCl}_2$  and  $\text{ZnCl}_2$  was quite



similar to that of  $\text{CaCl}_2$  in electric charge, leading to abnormal weight loss of the copolymer film, and the QCM frequency slightly increased to 3 Hz. This high  $\text{Ca}^{2+}$ -ion selectivity was further validated by a time-dependent dissipation curve, and the real-time information of the changes in viscoelasticity and thickness of the copolymer layer was recorded. As shown in Fig. 3b (red line), a

prominent dissipation increase ( $\Delta D$ :  $5.6 \times 10^{-6}$ ) was only observed for  $\text{CaCl}_2$  adsorption on the copolymer film. Based on the QCM adsorption theory<sup>54</sup>, a softer and swollen copolymer film after interacting with  $\text{CaCl}_2$  was demonstrated by these data, reflecting a relaxed state of the copolymer chains. By comparison, the NaCl, KCl,  $\text{ZnCl}_2$ , or  $\text{AlCl}_3$  adsorption-induced dissipation changes

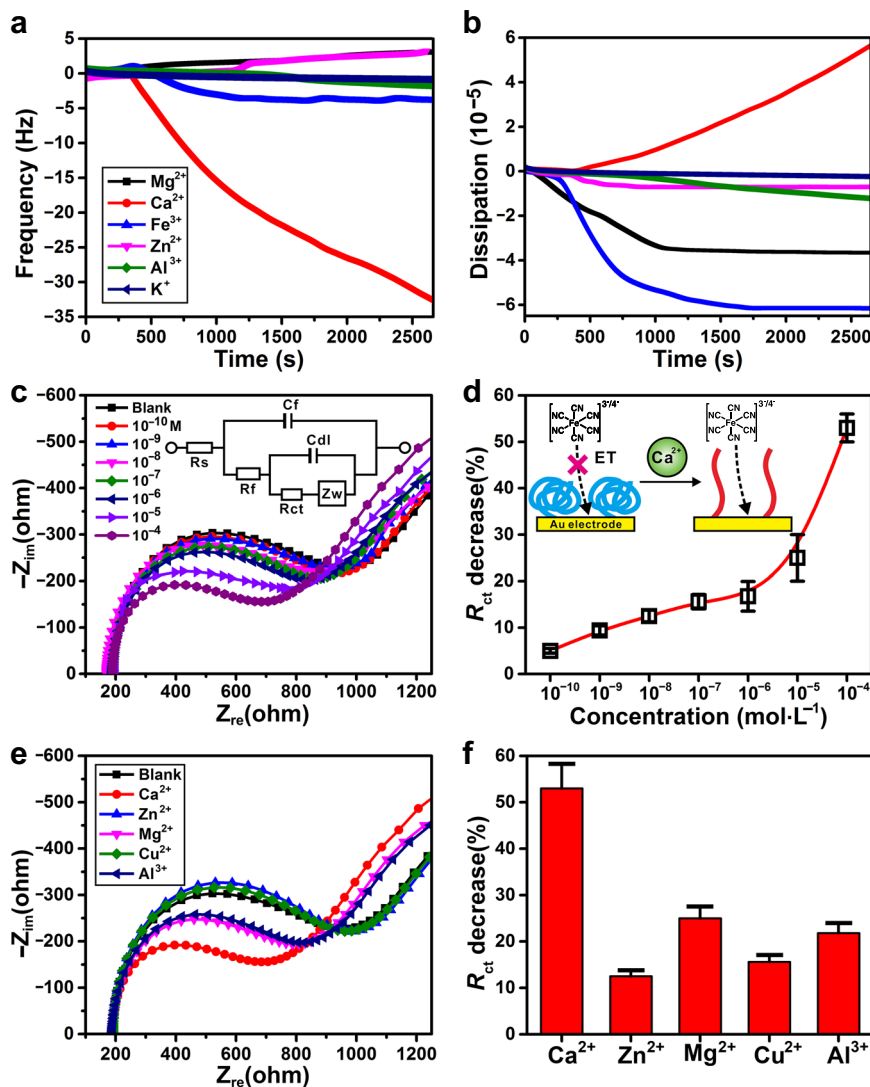


**Fig. 3** Specific adsorption and conformational transition of PNI-co-DDDEEK<sub>0.2</sub>-co-CF<sub>3</sub>-PT<sub>0.2</sub> copolymer film toward CaCl<sub>2</sub>, monitored by quartz crystal microbalance with dissipation (QCM-D) and electrochemical impedance spectroscopy (EIS). Time dependency of frequency **a** dissipation and **b** variations during MgCl<sub>2</sub>, CaCl<sub>2</sub>, FeCl<sub>3</sub>, ZnCl<sub>2</sub>, AlCl<sub>3</sub>, or KCl (10 μM in pure water) adsorbed on the copolymer-modified quartz crystal resonator surface at 20 °C. **c** Nyquist plots of EIS obtained at the copolymer-modified electrode surface in 0.1 M KCl solution containing 5 mM Fe(CN)<sub>6</sub><sup>3-/4-</sup> upon additions of CaCl<sub>2</sub> from 10<sup>-10</sup> to 10<sup>-4</sup> M. Inset, equivalent circuit of the electrochemical sensor to study the impedance spectra. **d** CaCl<sub>2</sub> concentration dependence of the impedance change ratio ( $R_{ct}$ ) of the copolymer-modified gold electrodes in 5 mM [Fe(CN)<sub>6</sub>]<sup>3-/4-</sup>. Inset: the Ca<sup>2+</sup>-triggered transition of the copolymer chains promoted the mass transport of [Fe(CN)<sub>6</sub>]<sup>3-/4-</sup> through the copolymer brush. **e** Nyquist plots of EIS obtained at the copolymer-modified electrode surface upon addition of different metal ion solutions (CaCl<sub>2</sub>, ZnCl<sub>2</sub>, MgCl<sub>2</sub>, CuCl<sub>2</sub>, or AlCl<sub>3</sub>; 0.1 mM). **f** Comparison of the  $R_{ct}$  decrease caused by the adsorption of different metal ions (0.1 mM). Error bars represent standard error measurements

were negligible. MgCl<sub>2</sub> or FeCl<sub>3</sub> adsorption led to a continuous decrease in the dissipation value ( $\Delta D$ :  $-3.6 \times 10^{-6}$  or  $-6.1 \times 10^{-6}$ ), revealing remarkable shrinkage of the copolymer film. Distinct adsorption dynamics of various metal ions on the copolymer surfaces and the corresponding dissipation curve variations demonstrated the excellent Ca<sup>2+</sup> selectivity of the copolymer film. The <sup>1</sup>H NMR titration experiment provided auxiliary evidence for

complexation between the copolymer and Ca<sup>2+</sup>, in which clear chemical shift changes of the carboxylic acids and amides of the copolymer were observed after the addition of CaCl<sub>2</sub> (Supplementary Fig. 2b in SI).

The shrinking-to-swelling transition of the copolymer brushes might strongly influence the electrochemical process on the surface of a copolymer-modified gold electrode, resulting in remarkable alteration of the mass



transport of  $[\text{Fe}(\text{CN})_6]^{3-/4-}$  through the copolymer brush, from bulk solution to the electrode surface (Inset of Fig. 3d)<sup>35</sup>. Based on this presumption, the  $\text{Ca}^{2+}$ -adsorption-induced conformational transition could be monitored by EIS. Figure 3c displays the Nyquist plots obtained for the copolymer-modified electrode before and after being treated with different amounts of  $\text{CaCl}_2$  in 5 mM  $\text{K}_3\text{Fe}(\text{CN})_6/\text{K}_4\text{Fe}(\text{CN})_6$  solution for 5 min. Initially, the electrochemical activity was blocked by the copolymer on the electrode with a charge transfer resistance ( $R_{\text{ct}}$ ) of 160  $\Omega$ , and this value gradually dropped down to 75  $\Omega$  when 100  $\mu\text{M}$  of  $\text{CaCl}_2$  was added. This  $R_{\text{ct}}$  decrease easily avoided the potential interference of nonspecific adsorption, which often results in the increase of  $R_{\text{ct}}$ . As shown in Fig. 3d, the  $R_{\text{ct}}$  value decreased gradually with the increasing  $\text{CaCl}_2$  concentration, and a 53%  $R_{\text{ct}}$  decrease was measured upon the addition of 100  $\mu\text{M}$  of  $\text{CaCl}_2$ . Notably, even when the concentration of  $\text{CaCl}_2$  was only 100 pM, the decrease in  $R_{\text{ct}}$  (5%) was still obvious and readily detected. In addition, the ion selectivity of the copolymer film was evaluated by EIS measurements, as shown in Fig. 3e, f. The most obvious changes in the Nyquist plot and corresponding  $R_{\text{ct}}$  were observed when  $\text{CaCl}_2$  (100  $\mu\text{M}$ ) was tested, while the  $\text{NaCl}$ ,  $\text{ZnCl}_2$ ,  $\text{MgCl}_2$ ,  $\text{CuCl}_2$ , or  $\text{AlCl}_3$ -induced  $R_{\text{ct}}$  changes were substantially weaker under the same conditions. These data further illustrated the highly selective response of the copolymer toward  $\text{CaCl}_2$ .

To construct biomimetic ionic nanochannels, PNI-*co*-CF<sub>3</sub>-PT<sub>0.2</sub>-*co*-DDDEEK<sub>0.2</sub> was grafted onto the porous channel of PAA membranes with uniform straight nanochannels (average pore size: 90–110 nm). The ATR-IR and thermal gravimetric analysis tests validated the modification of the copolymer on the PAA membrane (Supplementary Figs. 4 and 5 in SI). Then, atomic force microscopy (AFM) and scanning electron microscopy (SEM) were adopted to observe the morphological changes of the copolymer-modified PAA membranes after being immersed in a  $\text{CaCl}_2$  aqueous solution (20  $\mu\text{M}$ ) for 10 min. From the top view of the membrane, as observed by AFM (Fig. 4a, b), the initially well-defined nanopores became indistinct, and a few nanopores were blocked by the expanded copolymers according to the section profiles of the AFM images. According to the statistical analysis of the AFM images, the average pore size decreased from 82.5 to 52 nm, while the root mean square roughness ( $R_q$ ) of the PAA membrane increased from 7.23 to 10.85 nm, which indicated conspicuous macroscopic surface changes in the copolymer-modified PAA caused by  $\text{Ca}^{2+}$  adsorption. In addition, based on the SEM cross section images (Fig. 4c, d), the average wall thickness of the nanochannels increased from 55 to 81 nm, resulting in a remarkable decrease in the average size of the nanochannels from 67 to 40 nm. These obvious morphological

changes provided direct evidence for the expansion of the copolymer chains.

To analyze the elementary composition of the copolymer film, X-ray photoelectron spectroscopy (XPS) was performed. Compared with the XPS spectrum of the bare PAA membrane, signals of C 1s, N 1s, S 2p, and F 1s with binding energies of 285.0, 399.9, 168.4, and 689.0 eV, respectively, could be clearly observed for the copolymer-modified PAA membrane, which validated the successful immobilization of the copolymer on the PAA membrane. When the copolymer-modified membrane was treated with  $\text{CaCl}_2$  solution (20  $\mu\text{M}$ ) for 10 min and then rinsed with water, Ca 2p signals with binding energies of 347.3 and 350.8 eV appeared (Fig. 4e), which indicated that  $\text{Ca}^{2+}$  had been chemically adsorbed onto the copolymer film. From the perspective of C 1s signals,  $\text{Ca}^{2+}$ -adsorption remarkably strengthened the carbonyl signal of C 1s, as shown by the blue dashed lines in Fig. 4f, g, which is a contribution from chelation binding. In addition, the C–H, C–C and C–N signals of C 1s increased substantially, indicating that these functional groups were fully exposed due to the expansion of the copolymer chains<sup>55</sup>.

With the expansion of the copolymer chains, the size of the nanochannels decreased sharply, which further led to a decrease in the ionic flux of the nanochannels. This ionic transport property of the nanochannel was examined by current–voltage measurements using a Keithley 6487 picoammeter (Fig. 5a). All PAA membranes were separately mounted in an electrochemical cell (inset of Fig. 5a). A  $\text{NaCl}$  solution served as the electrolyte to measure the ionic current across the nanochannels at a constant volume of 1 mL<sup>56</sup>. The initial transmembrane ionic current was 100  $\mu\text{A}$  (at +0.2 V), indicating the good permeability of the copolymer-modified PAA membrane for ion transport. Then, electrolytes with different concentrations of  $\text{CaCl}_2$  were separately added to the cell exposed to the PAA membrane. Figure 5b displays the  $\text{CaCl}_2$  concentration dependence of the ionic current (at +0.2 V) change ratio [defined as  $(I - I_0)/I_0$ , where  $I_0$  is the initial current] for the bare, PNIPAAm and PNI-*co*-CF<sub>3</sub>-PT<sub>0.2</sub>-*co*-DDDEEK<sub>0.2</sub>-modified PAA membranes<sup>45</sup>. The detection range for  $\text{Ca}^{2+}$  extended from  $1 \times 10^{-4}$  mol L<sup>-1</sup> to an ultratrace level of  $1 \times 10^{-11}$  mol L<sup>-1</sup>, which fully covered the intracellular and extracellular  $\text{Ca}^{2+}$  /  $1 \times 10^{-8}$  to  $1 \times 10^{-3}$  mol L<sup>-1</sup><sup>57,58</sup> and makes it possible to further utilize this artificial nanochannel for medical treatment. For the copolymer-modified PAA membrane, an elegant negative correlation curve between  $(I - I_0)/I_0$  and the  $\text{Ca}^{2+}$  concentration was observed, suggesting the powerful and flexible regulatory capacity of  $\text{Ca}^{2+}$  for this nanochannel. The ionic current change ratio gradually increased from 12.3% at  $10^{-11}$  mol L<sup>-1</sup> to 47.5% at  $10^{-4}$  mol L<sup>-1</sup>, reflecting a satisfactory gating performance. In

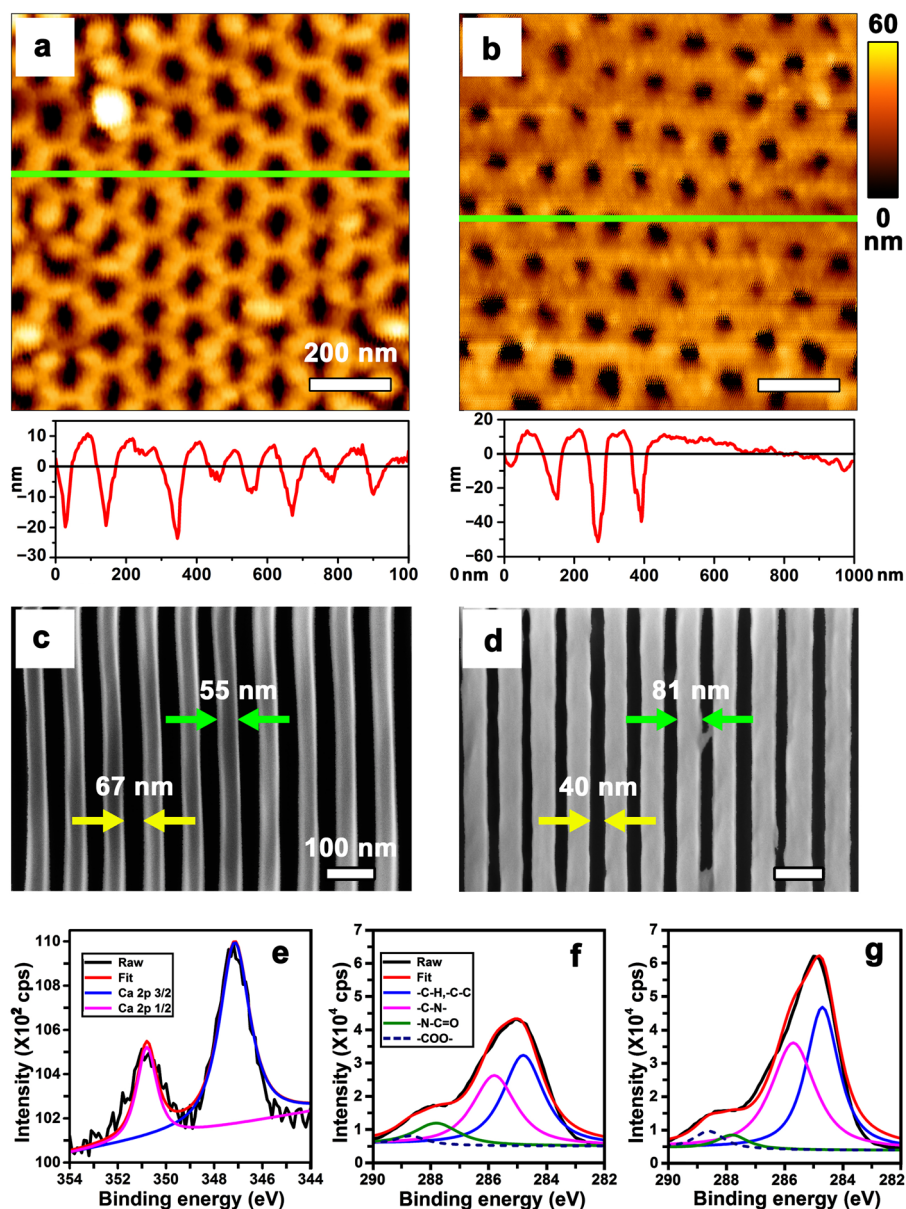
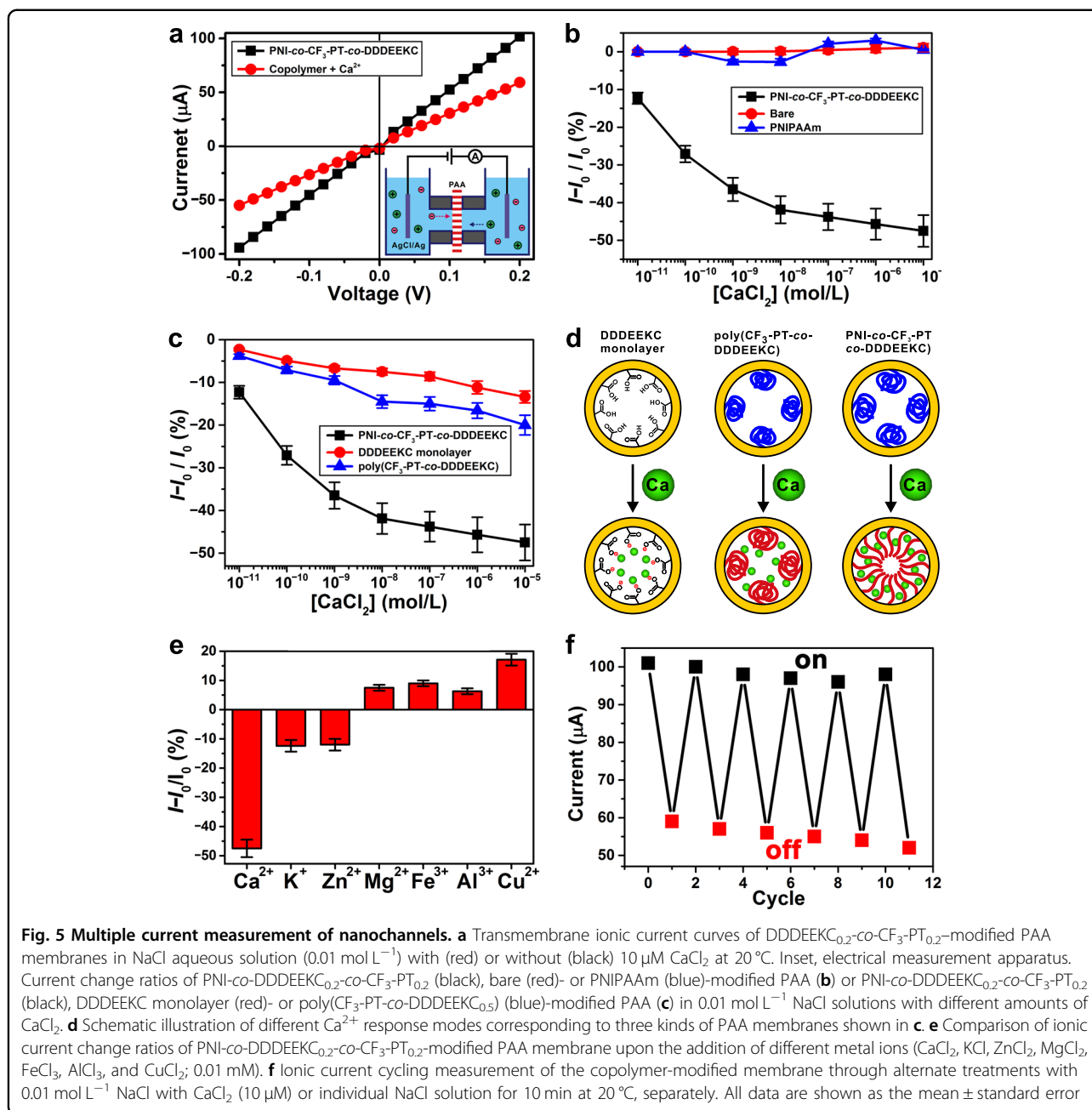


**Fig. 4** Atomic force microscopy (AFM) images. **a, b** and scanning electron microscopy (SEM) cross-sectional images (**c, d**) of the copolymer-modified porous anodic alumina (PAA) membrane (**a, c**) and after treatment with  $\text{CaCl}_2$  solutions (20  $\mu\text{M}$ ) for 10 min at 20  $^\circ\text{C}$  (**b, d**); green lines in the corresponding AFM section profiles. Narrow scan X-ray photoelectron spectra of the copolymer-modified PAA membrane before (**f**) and after (**e, g**) treatment with  $\text{CaCl}_2$  solution (20  $\mu\text{M}$ ) for 10 min at 20  $^\circ\text{C}$ . **e** Ca 2p; **f, g** C 1s. These surfaces were rinsed with water before measurements to eliminate the physical adsorption of  $\text{Ca}^{2+}$

contrast, a negligible change in the ionic current was observed for the bare or PNIPAAm-modified PAA, which indicated the strong  $\text{Ca}^{2+}$  binding capacity and high grafting density of the hepta-peptide in the three-component copolymer contributed to the remarkable sensibility and excellent gating efficiency.

A control experiment was performed to determine the rationality of the three-component copolymer design.

Using hepta-peptide single monolayer and poly( $\text{CF}_3\text{-PT-co-DDDEEK}_{0.5}$ )-modified PAA membranes, the maximal ionic current change ratios caused by  $\text{Ca}^{2+}$  were only 13.4% and 20%, respectively (Fig. 5c), both of which are substantially lower than that of PNI-*co*- $\text{CF}_3\text{-PT}_{0.2}\text{-co-DDDEEK}_{0.2}$ -modified PAA. We presumed that  $\text{Ca}^{2+}$  adsorption on the hepta-peptide monolayer surface only changed the surface charge of the nanochannels owing to



the chelation binding between Ca<sup>2+</sup> and the carboxylic acid groups in the hepta-peptide (Fig. 5d, left panel). For the poly(CF<sub>3</sub>-PT-co-DDDEEK<sub>0.5</sub>) two-component copolymer with the absence of PNIPAAm, the flexibility of the copolymer chains was substantially reduced, resulting in a more contracted state owing to strong hydrogen bonding interactions between CF<sub>3</sub>-PT and the hepta-peptide units. Under this condition, the introduction of Ca<sup>2+</sup> could not destroy such a compact hydrogen bond network, and the conformational change was limited

(Fig. 5d, middle panel). Only the integration of hepta-peptide, CF<sub>3</sub>-PT, and flexible PNIPAAm into one system allowed the Ca<sup>2+</sup>-triggered *globule-to-coil* transition of the copolymer to occur and contributed to the remarkable ionic current change (Fig. 5d, right panel).

Satisfactory reversibility of the ionic gating behaviors was also displayed. As shown in Fig. 5e, the ionic current switches between 100 and 50 μA through alternate treatment by the electrolyte with or without CaCl<sub>2</sub> (10 μM), and the reversibility was well maintained after seven cycles.

Due to the complexity of the cellular environment, a high demand is set not only for sensitivity and reversibility but also for selectivity of natural ion channels. Thus, the selectivity of an artificial nanochannel system is a vital evaluation criterion. A series of selectivity tests was performed using a control variable method. As expected, not only a sensitive and reversible response to the target  $\text{Ca}^{2+}$  was achieved; this nanochannel system also displayed accurate discrimination capacity among  $\text{Ca}^{2+}$ ,  $\text{K}^+$ ,  $\text{Zn}^{2+}$ ,  $\text{Mg}^{2+}$ ,  $\text{Fe}^{3+}$ ,  $\text{Al}^{3+}$ , and  $\text{Cu}^{2+}$  (Fig. 5f). The  $\text{Ca}^{2+}$  adsorption-induced ionic current change ratio (47.5%) was significantly larger than that of  $\text{K}^+$  (12.4%) or  $\text{Zn}^{2+}$  (12%) and was distinct from that of  $\text{Mg}^{2+}$ ,  $\text{Fe}^{3+}$ ,  $\text{Al}^{3+}$ , and  $\text{Cu}^{2+}$ , the adsorption of which led to an increase in the ionic current. This indicates the remarkable advantage of our material with a high specificity toward  $\text{Ca}^{2+}$  that conventional artificial nanochannels have difficulty achieving.

## Discussion

In conclusion, inspired by the CICR process, we constructed a smart (PNI-*co*-CF<sub>3</sub>-PT<sub>0.2</sub>-*co*-DDDEEK<sub>0.2</sub>)-based calcium-actuated nanochannel. With the intense conformational transitions of the copolymer chains from *globule* to *coil*, the gating behavior of the smart nanochannel is closer to that of an ion channel protein, facilitating sensitive monitoring of  $\text{Ca}^{2+}$  concentrations as low as 10 pM and achieving a wide stimulus response range to  $\text{Ca}^{2+}$  that fully covers  $\text{Ca}^{2+}$  levels in human cells. Excellent selectivity among various multivalent metal ions and satisfactory reversibility are attractive features, making it possible to recognize  $\text{Ca}^{2+}$  and modulate the gating of nanochannels in a complex environment. Moreover, this work demonstrates the feasibility of utilizing a biomimetic strategy for building artificial nanochannels with the help of biomolecule-responsive polymer design, which will give rise to more attractive work on biomimetic nanochannels.

In addition to  $\text{Ca}^{2+}$  channels, as one of the most widespread secondary messengers used in signal transduction,  $\text{Ca}^{2+}$  ions play key roles in the physiology and biochemistry of organisms and cells<sup>2</sup>. Particularly, the calcium levels in mammals are tightly regulated, and channels determine the release of  $\text{Ca}^{2+}$  from bone into bloodstream, reabsorption of  $\text{Ca}^{2+}$  in the kidney back into circulation, activation of vitamin D<sub>3</sub> to calcitriol capable of promoting calcium absorption, and participate in blood-clotting cascade and muscular contraction<sup>34</sup>. Therefore, the concentration of  $\text{Ca}^{2+}$  in the human body has become a vital index in research on tissue engineering and biomedicine<sup>59</sup>, increasing demand for  $\text{Ca}^{2+}$  detection and  $\text{Ca}^{2+}$  controllable release in interdisciplinary fields. In this context, our smart material may have potential applications in high-sensitivity  $\text{Ca}^{2+}$  detection and portable devices in therapy, as well as promising  $\text{Ca}^{2+}$ -actuated bioseparation membranes and microfluidic devices<sup>60</sup>.

## Acknowledgements

This work was supported by the National Natural Science Foundation of China (51473131, 51533007, and 21775116), DICP Innovation Funding (DICP-RC201801), and LiaoNing Revitalization Talents Program (XLYC1802109). G.Q. acknowledges Wuhan Morning Light Plan of Youth Science and Technology.

## Author details

<sup>1</sup>State Key Laboratory of Advanced Technology for Materials Synthesis and Processing, Wuhan University of Technology, 122 Luoshi Road, 430070 Wuhan, PR China. <sup>2</sup>Key Laboratory of Separation Science for Analytical Chemistry, Dalian Institute of Chemical Physics, Chinese Academy of Sciences, 457 Zhongshan Road, 116023 Dalian, PR China. <sup>3</sup>Research Centre of Modern Analytical Technology, Tianjin University of Science and Technology, Tianjin, PR China. <sup>4</sup>State Key Laboratory of Fine Chemicals, Institute of Artificial Photosynthesis, Dalian University of Technology, 116024 Dalian, PR China

## Conflict of interest

The authors declare that they have no conflict of interest.

## Publisher's note

Springer Nature remains neutral with regard to jurisdictional claims in published maps and institutional affiliations.

**Supplementary information** is available for this paper at <https://doi.org/10.1038/s41427-019-0148-4>.

Received: 26 February 2019 Revised: 29 May 2019 Accepted: 30 May 2019  
Published online: 30 August 2019

## References

- Noskov, S. Y., Bernèche, S. & Roux, B. Control of ion selectivity in potassium channels by electrostatic and dynamic properties of carbonyl ligands. *Nature* **431**, 830 (2004).
- Dong, Z., Saikumar, P., Weinberg, J. M. & Venkatchalam, M. A. Calcium in cell injury and death. *Annu. Rev. Pathol. Mech. Dis.* **1**, 405–434 (2006).
- Nonner, W., Catacuzzeno, L. & Eisenberg, B. Binding and selectivity in L-type calcium channels: a mean spherical approximation. *Biophys. J.* **79**, 1976–1992 (2000).
- Matulef, K. & Zagotta, W. N. Cyclic nucleotide-gated ion channels. *Annu. Rev. Cell Dev. Biol.* **19**, 23–44 (2003).
- Sun, Z. H., Barboiu, M., Legrand, Y. M., Petit, E. & Rotaru, A. Highly selective artificial cholesteryl crown ether  $\text{K}^+$  channels. *Angew. Chem. Int. Ed.* **54**, 14473–14477 (2015).
- Gao, Y., Szymonowski, J. E., Sun, X., Burns, P. C. & Liu, T. Thermal responsive ion selectivity of uranyl peroxide nanocages: an inorganic mimic of  $\text{K}^+$  ion channels. *Angew. Chem. Int. Ed.* **55**, 6887–6891 (2016).
- Guo, T., Gillespie, D. & Fill, M. Ryanodine receptor current amplitude controls  $\text{Ca}^{2+}$  sparks in cardiac muscle. *Circ. Res.* **111**, 28–36 (2012).
- Zalk, R. et al. Structure of a mammalian ryanodine receptor. *Nature* **517**, 44 (2014).
- Wei, R. et al. Structural insights into  $\text{Ca}^{2+}$ -activated long-range allosteric channel gating of RyR1. *Cell Res.* **26**, 977 (2016).
- Zhou, Q. et al. Impairment of PARK14-dependent  $\text{Ca}^{2+}$  signalling is a novel determinant of Parkinson's disease. *Nat. Commun.* **7**, 10332 (2016).
- Immler, R., Simon, S. I. & Sperandio, M. Calcium signalling and related ion channels in neutrophil recruitment and function. *Eur. J. Clin. Invest.* **48**, e12964 (2018).
- Hoffman, A. S. Stimuli-responsive polymers: biomedical applications and challenges for clinical translation. *Adv. Drug Deliv. Rev.* **65**, 10–16 (2013).
- Pérez-Mitta, G., Albesa, A. G., Trautmann, C., Toimil-Molares, M. E. & Azzaroni, O. Bioinspired integrated nanosystems based on solid-state nanopores: "ion-tronic" transduction of biological, chemical and physical stimuli. *Chem. Sci.* **8**, 890–913 (2017).
- Zhang, X. et al. Visual and highly sensitive detection of cancer cells by a colorimetric aptasensor based on cell-triggered cyclic enzymatic signal amplification. *Anal. Chem.* **86**, 5567–5572 (2014).



15. Siwy, Z. S., Powell, M. R., Kalman, E., Astumian, R. D. & Eisenberg, R. S. Negative incremental resistance induced by calcium in asymmetric nanopores. *Nano Lett.* **6**, 473–477 (2006).
16. Vilozny, B., Actis, P., Seger, R. A., Vallmajo-Martin, Q. & Pourmand, N. Reversible cation response with a protein-modified nanopipette. *Anal. Chem.* **83**, 6121–6126 (2011).
17. Ali, M. et al. Calcium binding and ionic conduction in single conical nanopores with polyacid chains: model and experiments. *ACS Nano*. **6**, 9247–9257 (2012).
18. Siwy, Z. S. et al. Calcium-induced voltage gating in single conical nanopores. *Nano Lett.* **6**, 1729–1734 (2006).
19. Powell, M. R. et al. Nanoprecipitation-assisted ion current oscillations. *Nat. Nanotechnol.* **3**, 51 (2007).
20. He, Y. et al. Tuning transport properties of nanofluidic devices with local charge inversion. *J. Am. Chem. Soc.* **131**, 5194–5202 (2009).
21. Meng, Z., Jiang, C., Li, X. & Zhai, J. Calcein-modified multichannels on PET films for calcium-responsive nanogating. *ACS Appl. Mater. Interfaces* **6**, 3794–3798 (2014).
22. Secker, C., Brosnan, S. M., Luxenhofer, R. & Schlaad, H. Poly( $\alpha$ -Peptoid) s revisited: synthesis, properties, and use as biomaterial. *Macromol. Biosci.* **15**, 881–891 (2015).
23. Wen, L. & Jiang, L. Bio-inspired smart gating nanochannels based on polymer films. *Sci. China Chem.* **54**, 1537 (2011).
24. Hou, X., Zhang, H. & Jiang, L. Building bio-inspired artificial functional nanochannels: from symmetric to asymmetric modification. *Angew. Chem. Int. Ed.* **51**, 5296–5307 (2012).
25. Guo, W., Tian, Y. & Jiang, L. Asymmetric ion transport through ion-channel-mimetic solid-state nanopores. *Acc. Chem. Res.* **46**, 2834–2846 (2013).
26. Cobo, I., Li, M., Sumerlin, B. S. & Perrier, S. Smart hybrid materials by conjugation of responsive polymers to biomacromolecules. *Nat. Mater.* **14**, 143 (2014).
27. Sun, Y. et al. A light-regulated host–guest-based nanochannel system inspired by channelrhodopsins protein. *Nat. Commun.* **8**, 260 (2017).
28. Sun, Z. et al. Fabrication of cysteine-responsive biomimetic single nanochannels by a thiol-yne reaction strategy and their application for sensing in urine samples. *Adv. Mater.* **26**, 455–460 (2014).
29. Mamad-Hemouch, H. et al. Biomimetic nanotubes based on cyclodextrins for ion-channel applications. *Nano Lett.* **15**, 7748–7754 (2015).
30. Huang, C., Yang, G., Ha, Q., Meng, J. & Wang, S. Multifunctional “smart” particles engineered from live immunocytes: toward capture and release of cancer cells. *Adv. Mater.* **27**, 310–313 (2015).
31. Li, X. et al. Integrated solid-state nanopore electrochemistry array for sensitive, specific, and label-free biodetection. *Langmuir* **34**, 14787–14795 (2018).
32. Li, L. et al. High Performance field-effect ammonia sensors based on a structured ultrathin organic semiconductor film. *Adv. Mater.* **25**, 3419–3425 (2013).
33. Li, W., Yang, C.-X. & Yan, X.-P. A versatile covalent organic framework-based platform for sensing biomolecules. *Chem. Commun.* **53**, 11469–11471 (2017).
34. Qing, G. & Sun, T. Chirality-triggered wettability switching on a smart polymer surface. *Adv. Mater.* **23**, 1615–1620 (2011).
35. Ding, S., Cao, S., Zhu, A. & Shi, G. Wettability switching of electrode for signal amplification: conversion of conformational change of stimuli-responsive polymer into enhanced electrochemical chiral analysis. *Anal. Chem.* **88**, 12219–12226 (2016).
36. Long, J. R., Shaw, W. J., Stayton, P. S. & Drobny, G. P. Structure and dynamics of hydrated statherin on hydroxyapatite as determined by solid-state NMR. *Biochemistry* **40**, 15451–15455 (2001).
37. Roy, D., Cambre, J. N. & Sumerlin, B. S. Future perspectives and recent advances in stimuli-responsive materials. *Prog. Polym. Sci.* **35**, 278–301 (2010).
38. Stuart, M. A. C. et al. Emerging applications of stimuli-responsive polymer materials. *Nat. Mater.* **9**, 101 (2010).
39. Masuda, H. & Fukuda, K. Ordered metal nanohole arrays made by a two-step replication of honeycomb structures of anodic alumina. *Science* **268**, 1466 (1995).
40. Yuan, J. H., He, F. Y., Sun, D. C. & Xia, X. H. A simple method for preparation of through-hole porous anodic alumina membrane. *Chem. Mater.* **16**, 1841–1844 (2004).
41. Wu, S. et al. Facile fabrication of nanofluidic diode membranes using anodic aluminium oxide. *Nanoscale* **4**, 5718–5723 (2012).
42. Zhang, Z. et al. A Bioinspired multifunctional heterogeneous membrane with ultrahigh ionic rectification and highly efficient selective ionic gating. *Adv. Mater.* **28**, 144–150 (2016).
43. Hui, C. M. et al. Surface-initiated polymerization as an enabling tool for multifunctional (nano-)engineered hybrid materials. *Chem. Mater.* **26**, 745–762 (2014).
44. Okuyama, H., Oshiba, Y., Ohashi, H. & Yamaguchi, T. Control of target molecular recognition in a small pore space with biomolecule-recognition gating membrane. *Small* **14**, 1702267 (2018).
45. Lu, Q. et al. Developing an inositol-phosphate-actuated nanochannel system by mimicking biological calcium ion channels. *ACS Appl. Mater. Interfaces* **9**, 32554–32564 (2017).
46. Roselin, L. S., Lin, M.-S., Lin, P.-H., Chang, Y. & Chen, W.-Y. Recent trends and some applications of isothermal titration calorimetry in biotechnology. *Biotech. J.* **5**, 85–98 (2010).
47. Raj, P. A., Johnsson, M., Levine, M. J., Nancollas, G. H. & Salivary, statherin Dependence on sequence, charge, hydrogen bonding potency, and helical conformation for adsorption to hydroxyapatite and inhibition of mineralization. *J. Biol. Chem.* **267**, 5968–5976 (1992).
48. Vacogne, C. D., Wei, C., Tauer, K. & Schlaad, H. Self-assembly of  $\alpha$ -helical polypeptides into microscopic and enantiomeric spirals. *J. Am. Chem. Soc.* **140**, 11387–11394 (2018).
49. Thordarson, P. Determining association constants from titration experiments in supramolecular chemistry. *Chem. Soc. Rev.* **40**, 1305–1323 (2011).
50. Caltagirone, C. & Gale, P. A. Anion receptor chemistry: highlights from 2007. *Chem. Soc. Rev.* **38**, 520–563 (2009).
51. Ragusa, A., Hayes, J. M., Light, M. E. & Kilburn, J. D. A combined computational and experimental approach for the analysis of the enantioselective potential of a new macrocyclic receptor for N-protected  $\alpha$ -amino acids. *Chemistry* **13**, 2717–2728 (2007).
52. Zhang, G. & Wu, C. Quartz crystal microbalance studies on conformational change of polymer chains at interface. *Macromol. Rapid Commun.* **30**, 328–335 (2009).
53. Sauerbrey, G. Verwendung von schwingquarzen zur wägung dünner schichten und zur mikrowägung. *Z. Phys.* **155**, 206–222 (1959).
54. Satoh, M., Kawashima, T. & Komiyama, J. Competitive counterion binding and dehydration of polyelectrolytes in aqueous solutions. *Polymer* **32**, 892–896 (1991).
55. Weng, Y. et al. Polyethyleneimine-modified graphene oxide nanocomposites for effective protein functionalization. *Nanoscale* **34**, 7 (2015).
56. Tian, Y. et al. A biomimetic zinc activated ion channel. *Chem. Commun.* **46**, 1682–1684 (2010).
57. Boittin, F.-X., Gribi, F., Serir, K. & Bény, J.-L.  $\text{Ca}^{2+}$ -independent PLA2 controls endothelial store-operated  $\text{Ca}^{2+}$  entry and vascular tone in intact aorta. *Am. J. Physiol. Heart Circ Physiol.* **295**, H2466–H2474 (2008).
58. Vig, M. et al. CRACM1 is a plasma membrane protein essential for store-operated  $\text{Ca}^{2+}$  entry. *Science* **312**, 1220 (2006).
59. Brini, M., Ottolini, D., Cali, T. & Carafoli, E. Neuronal calcium signaling: function and dysfunction. *Cell. Mol. Life Sci.* **15**, 2787–2814 (2014).
60. Zhang, Q. et al. Redox switch of ionic transport in conductive polypyrrole-engineered unipolar nanofluidic diodes. *Nano. Res.* **11**, 3715–3725 (2017).